11-2009

On Coupling a Lumped Parameter Heart Model and a Three-Dimensional Finite Element Aorta Model

H. J. Kim
Stanford University

Irene E. Vignon-Clementel
INRIA Paris-Rocquencourt

C. A. Figueroa
Stanford University

John F. LaDisa
Marquette University, john.ladisa@marquette.edu

K. E. Jansen
Rensselaer Polytechnic Institute

See next page for additional authors

On Coupling a Lumped Parameter Heart Model and a Three-Dimensional Finite Element Aorta Model

H. J. Kim
Department of Mechanical Engineering, Stanford University, Stanford, CA
I. E. Vignon-Clementel
INRIA, Paris-Rocquencourt, BP 105, 78153, Le Chesnay Cedex, France
C. A. Figueroa
Department of Bioengineering, Stanford University, Stanford, CA
J. F. LaDisa
Department of Biomedical Engineering, Marquette University, Milwaukee, WI
K. E. Jansen
Scientific Computation Research Center and the Department of Mechanical, Aeronautical and Nuclear Engineering, Rensselaer Polytechnic Institute, Troy, NY
J. A. Feinstein
Department of Bioengineering, Stanford University, Stanford, CA

Department of Pediatrics, Stanford University, Stanford, CA
C. A. Taylor
Department of Bioengineering, Stanford University, Stanford, CA
Department of Pediatrics, Stanford University, Stanford, CA
Department of Surgery, Stanford University, Stanford, CA

Abstract

Aortic flow and pressure result from the interactions between the heart and arterial system. In this work, we considered these interactions by utilizing a lumped parameter heart model as an inflow boundary condition for three-dimensional finite element simulations of aortic blood flow and vessel wall dynamics. The ventricular pressure–volume behavior of the lumped parameter heart model is approximated using a time varying elastance function scaled from a normalized elastance function. When the aortic valve is open, the coupled multidomain method is used to strongly couple the lumped parameter heart model and three-dimensional arterial models and compute ventricular volume, ventricular pressure, aortic flow, and aortic pressure. The shape of the velocity profiles of the inlet boundary and the outlet boundaries that experience retrograde flow are constrained to achieve a robust algorithm. When the aortic valve is closed, the inflow boundary condition is switched to a zero velocity Dirichlet condition. With this method, we obtain physiologically realistic aortic flow and pressure waveforms. We demonstrate this method in a patient-specific model of a normal human thoracic aorta under rest and exercise conditions and an aortic coarctation model under pre- and post-interventions.

Introduction

Computational simulations of blood flow are used to study the cardiovascular system in a variety of applications31 including the study of the hemodynamics of healthy and diseased blood vessels,3,18,30 the design and evaluation of vascular medical devices,15,28 the planning of vascular surgeries, and the prediction of the outcomes of the surgeries.16,26,32 With advances in computing power and numerical methods, such simulations are being extensively used for applications where experimental data are limited or unavailable.

However, due to the complex characteristics of the cardiovascular system, many challenges remain in quantifying realistic velocity and pressure fields. One of these challenges is the development of boundary conditions. Previously, we showed how the velocity and pressure fields of the same computational domain can change significantly depending on the choice of outflow boundary conditions.35 Outflow boundary conditions affect flow distribution, the range of the computed pressure, reflection and attenuation of the pressure wave, and the shape of the flow and pressure waveforms. In an effort to develop appropriate outflow boundary conditions, alternate methods to couple the computational domain with reduced-order zero-dimensional and one-dimensional analytic and numerical models have been proposed.5,16,19,35 We developed a new method, the coupled multidomain method, to couple outflow boundaries with simple analytic models such as a resistance, impedance, or 3-element Windkessel model, and obtained physiologically realistic flow rate and pressure fields in complex models.35

In contrast to developments made in the area of outflow boundary conditions, little progress has been reported for the development of an inflow boundary condition despite the fact that proximal to the inflow boundary, there is also an upstream part of the cardiovascular system that interacts with the computational domain. Conventionally, a flow or pressure waveform obtained from experiments is utilized as an inflow boundary condition. In consequence, the bidirectional interactions between the downstream computational domain and the upstream portion of the cardiovascular system are ignored. Furthermore, when using prescribed flow or pressure waveforms, the utilized inflow boundary condition is only valid for one particular physiologic condition.

To simulate a different physiologic condition, a different inflow boundary condition must be assigned. Without experimental data available for different physiologic conditions, a different flow or pressure waveform needs to be constructed based on available literature data.

Fundamentally, aortic blood flow and pressure result from the interactions between the heart and arterial system. The aortic flow and pressure change as the cardiac properties change and vice versa. To study how the changes in cardiac properties and arterial system influence each other, the inflow boundary condition should model the interactions between them. For example, to treat a failing heart, physicians can either provide the patient with an inotrope to enhance the contractility of the heart or vasodilators, which reduce the afterload of the heart.1 These treatment options will change both the aortic flow and pressure and the cardiac properties due to the interactions between them. To predict the outcome of the treatment satisfactorily, it is essential to understand the interactions between the heart and arterial system.

A variety of heart models ranging from lumped parameter to three-dimensional models have been developed to simulate the relaxation, filling, contraction, and ejection phases of the heart.10,11,17,21,24,29 In particular, lumped parameter heart models approximate global characteristics of the heart using simple hydraulic models of a resistance, capacitance, inductance, pressure source, and diode, resulting in time-varying ordinary differential equations of flow and pressure. Several previous studies have utilized these lumped parameter heart models to calculate aortic flow and pressure using lumped parameter, one-dimensional and three-dimensional models of the aorta.6,16,17,24 However, for previous work with three-dimensional aortic models, the coupling between the computational domain and lumped parameter heart model was explicit and the simulations were computed with the assumption of rigid vessel walls.

In this paper, we used the coupled multidomain method35 to implicitly couple a lumped parameter heart model24 to a subject-specific three-dimensional finite element model of the aorta. We utilized an augmented Lagrangian method to enforce constraints on the shape of the velocity profiles on the inlet boundary and outlet boundaries that experience retrograde flow.12 Using this implicit coupling method along with the constraints on the velocity profile shape, we greatly increased the realism of three-dimensional aortic blood flow simulations coupled to a lumped parameter heart model. We also incorporated deformable wall properties of the blood vessels using the coupled momentum method.4

This paper is organized as follows. First, we present a method for strongly coupling a lumped parameter heart model to a three-dimensional finite element model of the aorta. We then demonstrate this method by applying it to simulations of blood flow in a subject-specific thoracic aorta model to study changes in cardiac properties and aortic flow and pressure for rest and light exercise conditions. Finally, we demonstrate the utility of this method by applying it to compute the reduction in cardiac load when comparing the pre-intervention and post-intervention hemodynamic conditions of a subject-specific thoracic aorta model with an aortic coarctation.

Methods

Three-Dimensional Finite Element Simulations of Blood Flow and Vessel Wall Dynamics

Blood flow in the large vessels of the cardiovascular system can be represented as a Newtonian fluid.18 The vessel walls can be approximated using a linear elastic model within the physiologic range of pulse pressure. The governing equations for the fluid consist of the incompressible Navier–Stokes equations, whereas the motion of the vessel wall is governed by the elastodynamics equations. Initial and boundary conditions as well as fluid–solid interface conditions are required for the fluid and solid domains. In the method described herein, we assume a fixed fluid mesh and small displacements of the vessel wall.

For fluid domain Ω with its boundary Γ and solid domain Ω^s with its boundary Γ^s, the following equations are solved for velocities v⃗ ,v→, pressure *p*, and wall displacement u⃗ u→.4

Given $\vec{f}:\Omega \times (0,T) \to \mathcal{R}^3, \vec{f}^s:\Omega^s \times (0,T) \to \mathcal{R}^3, \vec{g}:\Gamma_g \times (0,T) \to \mathcal{R}^3, \vec{g}^s:\Gamma_g^s \times (0,T) \to \mathcal{R}^3, \vec{v}_0:\Omega \to \mathcal{R}^3, \vec{u}_0:\Omega^s \to \mathcal{R}^3$and $\vec{u}_{0,t}:\Omega^s \to \mathcal{R}^3$, find $\vec{v}(\vec{x},t), p(\vec{x},t)$, and $\vec{u}(\vec{x}^s,t) \forall \vec{x} \in \Omega, \forall \vec{x}^s \in \Omega^s, \forall t \in (0,T)$ such that the following is satisfied:

$$\begin{aligned}
\rho\vec{v}_{,t} + \rho\vec{v}\cdot\nabla\vec{v} &= -\nabla p + div(\underset{\sim}{\tau}) + \vec{f} \text{for} (\vec{x},t) \in \Omega \times (0,T) \\
div(\vec{v}) &= 0 \text{for} (\vec{x},t) \in \Omega \times (0,T) \\
\rho^s\vec{u}_{,tt} &= \nabla\cdot\underset{\sim}{\sigma}^s + \vec{f}^s \text{for} (\vec{x}^s,t) \in \Omega^s \times (0,T) \\
\text{where} \underset{\sim}{\tau} &= \mu(\nabla\vec{v} + (\nabla\vec{v})^T) \\
\text{and } \underset{\sim}{\sigma}^s &= \underset{\sim}{C}:\frac{1}{2}(\nabla\vec{u} + (\nabla\vec{u})^T)
\end{aligned}$$

(1)

with Dirichlet boundary conditions:

$$\begin{aligned}
\vec{v}(\vec{x},t) &= \vec{g}(\vec{x},t) \text{for} (\vec{x},t) \in \Gamma_g \times (0,T) \\
\vec{u}(\vec{x}^s,t) &= \vec{g}^s(\vec{x}^s,t) \text{for} (\vec{x}^s,t) \in \Gamma_g^s \times (0,T)
\end{aligned}$$

(2)

Neumann boundary condition:

$$\vec{t}_{\vec{n}} = [-p\underset{\sim}{I} + \underset{\sim}{\tau}]\vec{n} = \vec{h}(\vec{v},p,\vec{x},t) \text{for} (\vec{x},t) \in \Gamma_h \times (0,T)$$

(3)

fluid–solid interface condition:

$$\vec{t}_{\vec{n}} = \underset{\sim}{\sigma}^s\vec{n} = \vec{h}^s(\vec{v},p,\vec{x},t) \text{for} (\vec{x},t) \in \Gamma_h^s \times (0,T)$$

(4)

and initial conditions:

$$\begin{aligned}
\vec{v}(\vec{x},0) &= \vec{v}_0(\vec{x}) \text{for} \vec{x} \in \Omega \\
\vec{u}(\vec{x}^s,0) &= \vec{u}_0(\vec{x}^s) \text{for} \vec{x}^s \in \Omega^s \\
\vec{u}_{,t}(\vec{x}^s,0) &= \vec{u}_{0,t}(\vec{x}^s) \text{for} \vec{x}^s \in \Omega^s
\end{aligned}$$

(5)

Density ρ and dynamic viscosity μ of the blood and density ρ^s of the vessel walls are assumed to be constant. $\underset{\sim}{C}$ is a fourth-order tensor of material constants. Additionally, $\vec{f}$ is the external body force on the fluid domain, and $\vec{f}^s$ is the external body force on the solid domain.

The boundary Γ of the fluid domain is divided into Dirichlet boundary portion Γ_g and Neumann boundary portion Γ_h. These boundaries satisfy $\overline{(\Gamma_g \cup \Gamma_h)} = \Gamma$ and $\Gamma_g \cap \Gamma_h = \phi$.. Note that for this study, when the aortic valve is open, the inlet boundary is included in the Neumann boundary portion Γ_h, not in the Dirichlet boundary portion Γ_g to enable coupling with a lumped parameter heart model. Therefore, the Dirichlet boundary portion Γ_g only consists of the inlet and outlet rings of the computational domain when the aortic valve is open. In what follows, these rings are fixed in time and space.4

The Neumann boundary portion Γ_h consists of the inlet and outlet surfaces of the computational domain when the aortic valve is open. We divide the Neumann boundary portion Γ_h into inlet surface Γ_{in} and the set of all the outlet surfaces, Γ_h', such that $\overline{(\Gamma_{\text{in}} \cup \Gamma_h')} = \Gamma_h$ and $\Gamma_{\text{in}} \cap \Gamma_h' = \phi$.. For the outlet boundaries, we utilize the coupled multidomain method35 to prescribe the impedance of lumped parameter models approximating the downstream vasculature networks of the cardiovascular system not included in the computational model. The lateral surface of the fluid domain coincides with a membrane approximation for the vessel wall as modeled using the coupled momentum method for fluid–solid interaction.4 In this work, the coupled multidomain method is used on inlet surface Γ_{in} to couple a lumped parameter heart model to the computational domain. Similar to the treatment of the outflow boundary conditions, in this method, a lumped parameter heart model is used to define the operators $M = [\underset{\sim}{M}_m, \vec{M}_c]_{\Gamma_{\text{in}}}$ and $H = [\underset{\sim}{H}_m, \vec{H}_c]_{\Gamma_{\text{in}}}$ which approximate the traction and velocity fields of the inlet surface:

$$\begin{aligned} (-p\underset{\sim}{I} + \underset{\sim}{\tau})|_{\Gamma_{\text{in}}} &\approx [\underset{\sim}{M}_m(\vec{v}, p) + \underset{\sim}{H}_m]_{\Gamma_{\text{in}}} \\ \vec{v}|_{\Gamma_{\text{in}}} &\approx [\vec{M}_c(\vec{v}, p) + \vec{H}_c]_{\Gamma_{\text{in}}} \end{aligned}$$

(6)

Then, the resulting weak form is as follows:

$$\begin{aligned} &\int_\Omega \{\vec{w} \cdot (\rho \vec{v}_{,t} + \rho \vec{v} \cdot \nabla \vec{v} - \vec{f}) + \nabla \vec{w} : (-p\underset{\sim}{I} + \underset{\sim}{\tau})\} d\vec{x} - \int_\Omega \nabla q \cdot \vec{v} d\vec{x} \\ &+\zeta \int_{\Gamma^s} \{\vec{w} \cdot \rho^s \vec{v}_{,t} + \nabla \vec{w} : \underset{\sim}{\sigma}^s(\vec{u})\} ds - \zeta \int_{\partial \Gamma_h} \vec{w} \cdot \vec{h}^s dl + \int_{\Gamma^s} q\vec{v} \cdot \vec{n} ds \\ &- \int_{\Gamma_h'} \vec{w} \cdot \vec{h} ds + \int_{\Gamma_h'} q\vec{v} \cdot \vec{n} ds + \int_{\Gamma - \Gamma_h} q\vec{v} \cdot \vec{n} ds \\ &- \int_{\Gamma_{\text{in}}} \vec{w} \cdot (\underset{\sim}{M}_m(\vec{v}, p) + \underset{\sim}{H}_m) \cdot \vec{n} ds + \int_{\Gamma_{\text{in}}} q(\vec{M}_c(\vec{v}, p) + \vec{H}_c) \cdot \vec{n} ds = 0 \end{aligned}$$

(7)

where ζ is the wall thickness. The boxed terms now couple the lumped parameter heart model to the computational domain using the operators, *M* and *H* that are specific to the lumped parameter heart model, which is described below.

A stabilized semi-discrete finite element method was employed based on the ideas developed in Brooks and Hughes,2 Franca and Frey,7 Taylor *et al*.,33 and Whiting *et al*.36

Time-Varying Elastance Function

The contraction and relaxation of a ventricle is approximated using a time-varying elastance function.25,29 Elastance is the instantaneous ratio of ventricular pressure $P_v(t)$ and ventricular volume $V_v(t)$ according to the following equation:

$$P_v(t) = E(t) \cdot [V_v(t) - V_0]$$

(8)

Here, V_0 is a constant correction volume, which is recovered when the ventricle is unloaded.

Each subject has a different time-varying elastance function depending on his or her contractility, vascular loading, heart rate, etc. However, if the elastance function is normalized with a maximum elastance value, and t_{max}, the time difference between the onset of systole and the time at the maximum elastance value, the same normalized elastance function is obtained regardless of contractility, vascular loading, heart rate, and heart diseases.25,29 This normalized elastance function is scaled to approximate the measured cardiac output, pulse pressure, and contractility of each subject.

Lumped Parameter Heart Model Used to Define Operators

A lumped parameter heart model coupled to an inlet surface is shown in Fig. 1.24 For this study, we only consider the left side of the heart, but the same method can be applied to the right side of the heart. The heart model consists of constant left atrial pressure P_{LA}, mitral valve, atrio-ventricular valvular resistance $R_{A\text{-}V}$, atrio-ventricular inductance $L_{A\text{-}V}$, aortic valve, ventriculo-arterial valvular resistance $R_{V\text{-}art}$, ventriculo-arterial inductance $L_{V\text{-}art}$, and left ventricular pressure. The left ventricular pressure is modeled with time-varying elastance $E(t)$. An atrio-ventricular inductance $L_{A\text{-}V}$ and ventriculo-arterial inductance $L_{V\text{-}art}$ were added to the model proposed by Segers *et al*.24 in order to simulate the inertial effects of blood flow.

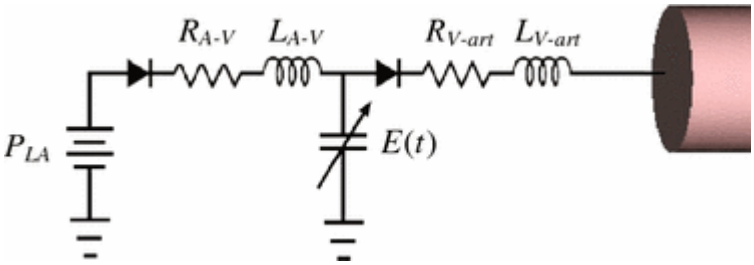

Figure 1 Lumped parameter heart model.24

In systole, when the left ventricular pressure rises above the aortic pressure, the aortic valve opens and enables the interactions between the ventricle and the arterial system (Fig. 2). During this phase, aortic flow and pressure arise naturally through the interactions between the lumped parameter heart model and the three-dimensional finite element model of the aorta. In diastole, when the aortic flow is reversed, the aortic valve closes. There is no aortic inflow from the ventricle during this phase. Ventricular pressure and volume are determined independently of the three-dimensional finite element model of the aorta, and are a function of the time-varying elastance function and the lumped parameter heart model. The ventricular pressure decreases as the ventricle is relaxed in diastole. When the ventricular pressure falls below the left atrial pressure, the mitral valve opens and the left atrial flow and left ventricular pressure are determined by the interactions between the left ventricle and the left atrium. The mitral valve closes when the left atrial flow is reversed (Fig. 2).

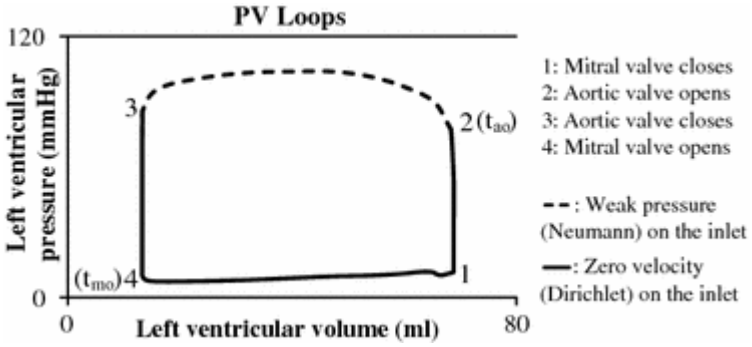

Figure 2 Pressure–volume loop of the left ventricle for a single cardiac cycle. Note that a weak pressure boundary condition on the inlet is assigned only when the aortic valve is open. When the aortic valve is closed, a zero velocity boundary condition is applied on the inlet

When the aortic valve is open, aortic flow is a function of the aortic pressure and ventricular pressure. Moreover, aortic flow is coupled to the ventricular volume as the ventricle ejects blood to the aorta. Thus, using the lumped parameter heart model described above, aortic flow $Q(t)$ is coupled to aortic pressure $P(t)$, ventricular volume $V_v(t)$, and the time-varying elastance function $E(t)$ through the following equation:

$$\begin{aligned} P(t) &= E(t)\cdot\{V_v(t)-V_0\} - Q(t)\cdot R_{\mathrm{V-art}} - \frac{dQ}{dt}\cdot L_{\mathrm{V-art}} \\ &= E(t)\cdot\{V_v(t_{\mathrm{ao}}) - \int_{t_{\mathrm{ao}}}^{t} Q(s)ds - V_0\} - Q(t)\cdot R_{\mathrm{V-art}} - \frac{dQ}{dt}\cdot L_{\mathrm{V-art}} \end{aligned}$$

(9)

where t_{ao} is the time the aortic valve opens.

Using this equation, the operators M and H are defined as follows:

$$\begin{aligned} [\underset{\sim}{M}_m(\vec{v},p) + \underset{\sim}{H}_m]_{\Gamma_{\mathrm{in}}} &= -E(t)\cdot\{V_v(t_{\mathrm{ao}}) + \int_{t_{\mathrm{ao}}}^{t} \int_{\Gamma_{\mathrm{in}}} \vec{v}\cdot\vec{n}d\Gamma ds - V_0\}\underset{\sim}{I} \\ &\quad -(R_{\mathrm{V-art}} + L_{\mathrm{V-art}}\frac{d}{dt})\int_{\Gamma_{\mathrm{in}}} \vec{v}\cdot\vec{n}d\Gamma\,\underset{\sim}{I} + \underset{\sim}{\tau} - (\vec{n}\cdot\underset{\sim}{\tau}\cdot\vec{n})\underset{\sim}{I} \\ [\vec{M}_c(\vec{v},p) + \vec{H}_c]_{\Gamma_{\mathrm{in}}} &= \vec{v}|_{\Gamma_{\mathrm{in}}} \end{aligned}$$

(10)

Using these operators, the traction and velocity fields of the inlet surface of the aortic model are now strongly coupled to the lumped parameter heart model and solved implicitly while the aortic valve is open.

When the mitral valve is open, atrial flow is a function of left atrial pressure P_{LA} and the left ventricular pressure, which is coupled to the left ventricular volume. The atrial flow $Q_{LA}(t)$ is computed through the following equation:

$$\begin{aligned} P_{\mathrm{LA}} &= E(t)\cdot\{V_v(t)-V_0\} + Q_{\mathrm{LA}}(t)\cdot R_{\mathrm{A-V}} + \frac{dQ_{\mathrm{LA}}}{dt}\cdot L_{\mathrm{A-V}} \\ &= E(t)\cdot\{V_v(t_{\mathrm{mo}}) + \int_{t_{\mathrm{mo}}}^{t} Q_{\mathrm{LA}}(s)ds - V_0\} + Q_{\mathrm{LA}}(t)\cdot R_{\mathrm{A-V}} + \frac{dQ_{\mathrm{LA}}}{dt}\cdot L_{\mathrm{A-V}} \end{aligned}$$

(11)

where t_{mo} is the time the mitral valve opens.

Opening and Closure of the Aortic Valve

The heart model is always coupled to the three-dimensional finite element model of the aorta but the interactions between the heart model and the aorta occur only when the aortic valve is open. In diastole and part of systole, the aortic valve remains closed, thus, there is no flow from the ventricle. To accommodate this change, the inlet boundary is switched from a Neumann boundary to Dirichlet boundary when there is no flow (Fig. 2). When the ventricular pressure rises above the aortic pressure again, the inlet boundary changes back from a Dirichlet boundary to a Neumann boundary. Finally, the boundary changes back to a Dirichlet boundary when there is retrograde aortic flow.

Constraints on the Shape of the Velocity Profiles of the Inlet and the Outlets with Retrograde Flow

In our approach, we weakly enforce boundary conditions such that the normal traction is a function of the flow rate using the coupled multidomain method.35 If the shape of the inlet velocity profile is free of constraints, it often results in an irregular profile prone to numerical instability. To resolve this issue, an augmented Lagrangian method was used to weakly enforce a shape of the inlet velocity profile as was done for retrograde outlet flows in Kim *et al*.12 The following axisymmetric velocity profile is prescribed after constructing a circular shape for the inlet surface:

$$v_n(\cdot,t) = \overline{v}(t) \times \frac{n+2}{n}\left(1-\left(\frac{r}{R}\right)^n\right)$$

(12)

where v_n is a normal velocity, $\bar{v}(t)\bar{v}(t)$ is the mean normal velocity, r is the distance between a point on the constrained surface and the center of the surface and R is the radius of the constrained surface. In-plane velocities are zeroed out weakly using additional constraints. A profile order n is chosen to approximate a parabolic (n = 2) or increasingly flat velocity profile based on the measured inflow waveform, inlet radius, and cardiac cycle. If the outlets have retrograde flow, constraints with the same profile order are enforced on the shape of the outlet velocity profiles to achieve a robust algorithm. The assumption of circular faces and the above choice of profile function were made without loss of generality.

Setting Up Initial Conditions Using Reduced-Order Models

To determine an appropriate initial condition, the three-dimensional finite element model of the aorta was replaced with a 3-element Windkessel model and run until a converged solution was obtained. Based on this converged solution describing a full cardiac cycle, one time point was selected and set as an initial condition for the lumped parameter heart model and the aortic flow and pressure of the three-dimensional finite element model of the aorta.

Choice of the Parameter Values of the Lumped Parameter Heart Model

The parameter values of the lumped parameter heart model were optimized to approximate the measured cardiac output and pulse pressure. Initially, the following parameter values were chosen based on measured values and literature data.17,23

$$t_{\max} = \begin{cases} \frac{T}{3}, & \text{at rest, where } T \text{ is the measured cardiac cycle.} \\ 0.5T, & \text{during exercise.} \end{cases}$$

$E_{\max} = \frac{\gamma \cdot R}{T}$, where R is the total resistance of the systemic circulation and $1 \leq \gamma \leq 2$.

$V_0 = V_{\text{esv}} - \frac{0.9P_{\text{sys}}}{E_{\max}}$, where V_{esv} is an end-systolic volume and P_{sys} is a systolic pressure.

$R_{\text{V-art}} = 10 \text{dyness/cm}^5$

$R_{\text{A-V}} = 10 \text{dyness/cm}^5$

$L_{\text{V-art}} = 0.6879 \text{dyness}^2/\text{cm}^5$

$L_{\text{A-V}} = 0.6670 \text{dyness}^2/\text{cm}^5$

E_{max} and V_0 were modified iteratively to minimize the difference between the computed cardiac output and pulse pressure and the measured cardiac output and pulse pressure based first on the simulation results of the lumped models and then the three-dimensional finite element solver. The iterations were continued until the computed cardiac output, pulse pressure, and flow distribution to each outlet matched the target subject-specific data within 5.0% relative difference.

Simulation Details

For the simulations presented here, we assumed that blood can be described as a Newtonian fluid with a density of 1.06 g/cm^3 and a dynamic viscosity of 0.04 dynes/cm^2 s. As a first approximation, we assumed that the blood vessel walls can be modeled as a linear elastic material with Poisson's ratio of 0.5, a wall density of 1.0 g/cm^3, and a wall thickness of 0.1 cm. The values of these material parameters are all physiologically reasonable. We utilized anisotropic finite element mesh generation techniques with refinement on the exterior surfaces and five boundary layers.20 The solutions were run until the relative changes in pressure fields at the inlet and the outlets were smaller than 1.0% compared to the solutions from the previous cardiac cycle.

The computer models used in the simulations were constructed from magnetic resonance imaging data. Each model started from the root of the aorta, ended above the diaphragm, and included the main upper branch vessels: right subclavian, left subclavian, right carotid, and left carotid arteries. For the inlet, we coupled the lumped parameter heart model described before. For the outlets, we assigned three-element Windkessel models to represent the downstream vasculature networks that are absent in the three-dimensional computational domains. Flow distribution to each outlet was based on data measured using cine phase contrast magnetic resonance imaging (cine PC-MRI) and literature data.37 Boundary conditions were adjusted to match both the flow distribution and the measured brachial artery pulse pressure.14,27 For a normal thoracic aorta model, we attempted to match the brachial pulse pressure at the level of the descending thoracic aorta based on the experiments conducted by Hope *et al.*,9 which demonstrated that brachial pressure is in the same range of the aortic pressure at the level of the diaphragm for normal subjects.

Results

A Subject-Specific Thoracic Aorta Model at Rest and During Exercise

In these simulations, we studied how cardiac properties change as the resistance of the lower extremities decreases due to the increase of flow demand during light exercise. A subject-specific thoracic aorta computer model of an eleven-year-old male subject was constructed (Fig. 3). Solutions were obtained using a 1,916,167 element and 345,069 node mesh with a time step size of 0.16 ms to simulate a resting condition and 0.1 ms to simulate a light exercise condition. The shape of the velocity profiles of the inlet and of all the outlets were constrained to an axisymmetric shape with a profile order of seven. To simulate light exercise, the resistance

value of the descending thoracic aorta was decreased in order to increase flow to the lower extremities. The cardiac cycle was shortened to simulate increased heart rate until the systolic pressure matched the systolic pressure of the resting state in the thoracic aorta. For simplicity, the boundary conditions of the upper branch vessels were unchanged. The parameter values of the Windkessel models are shown in Fig. 3 along with the time-varying elastance function and the parameter values of the lumped parameter heart model. The same time-varying elastance function was used for both rest and light exercise conditions.

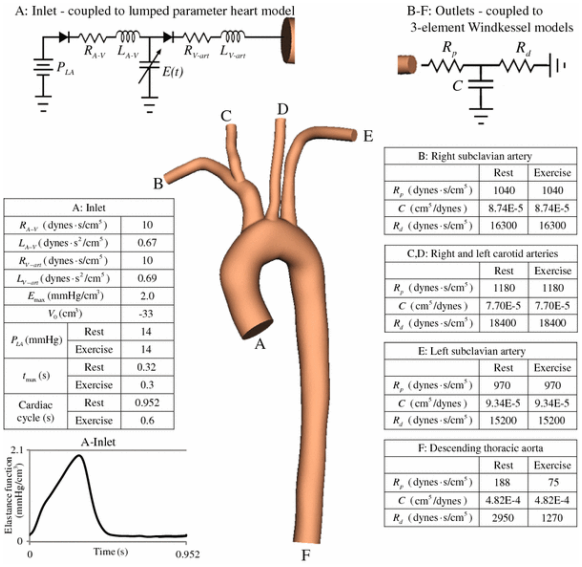

A: Inlet		
$R_{A\text{-}V}$ (dynes·s/cm^5)		10
$L_{A\text{-}V}$ (dynes·s^2/cm^5)		0.67
$R_{V\text{-}art}$ (dynes·s/cm^5)		10
$L_{V\text{-}art}$ (dynes·s^2/cm^5)		0.69
E_{max} (mmHg/cm^3)		2.0
V_0 (cm^3)		-33
P_{LA} (mmHg)	Rest	14
	Exercise	14
t_{max} (s)	Rest	0.32
	Exercise	0.3
Cardiac cycle (s)	Rest	0.952
	Exercise	0.6

B: Right subclavian artery	Rest	Exercise
R_p (dynes·s/cm^5)	1040	1040
C (cm^5/dynes)	8.74E-5	8.74E-5
R_d (dynes·s/cm^5)	16300	16300

C,D: Right and left carotid arteries	Rest	Exercise
R_p (dynes·s/cm^5)	1180	1180
C (cm^5/dynes)	7.70E-5	7.70E-5
R_d (dynes·s/cm^5)	18400	18400

E: Left subclavian artery	Rest	Exercise
R_p (dynes·s/cm^5)	970	970
C (cm^5/dynes)	9.34E-5	9.34E-5
R_d (dynes·s/cm^5)	15200	15200

F: Descending thoracic aorta	Rest	Exercise
R_p (dynes·s/cm^5)	188	75
C (cm^5/dynes)	4.82E-4	4.82E-4
R_d (dynes·s/cm^5)	2950	1270

Figure 3 Problem specification for simulations of blood flow in a normal thoracic aorta model under rest and exercise conditions

Wall deformability was also modeled. A Young's modulus of the vessel walls was chosen to be 6.04×10^6 dynes/cm^2 so that a maximum deformation of 11% was obtained based on cine PC-MRI data at the level of the ascending and descending thoracic aorta. The same value of Young's modulus was used for the exercise simulation. The simulations were run for a total of six cardiac cycles until the flow rate and pressure fields yielded periodic solutions.

In Fig. 4, computed pressure and flow waveforms of the inlet and the outlets are shown for rest and exercise conditions. The pressure–volume loops of the left ventricle for both conditions are also shown. The measured cardiac output of the subject was 3.4 L/min for the resting condition. The computed cardiac output of the subject was 3.5 L/min for the resting condition and 6.4 L/min during exercise. These values for rest and exercise are within the normal cardiac indices for children when scaled to body surface area.22 The body surface area of this subject was 1.45 m^2 and the cardiac index was 2.41 L/min/m^2 for the resting condition and 4.41 L/min/m^2 during exercise. The estimated cardiac output based on these cardiac indices was 3.5 L/min for a resting condition and 6.4 L/min for an exercise condition, respectively. The measured brachial pulse pressure of the subject at rest ranged from 63 to 106 mmHg. The computed brachial pulse pressure of the subject ranged from 62 to 106 mmHg for the resting condition and from 65 to 103 mmHg for the light exercise condition. The computed left ventricular pressure ranged from 7 to 104 mmHg for the resting condition and from 8 to 109 mmHg for the light exercise condition. The stroke volume was 56 cm^3 for the resting condition and 64 cm^3 for the light exercise condition (see Fig. 4). Increase in the cardiac output was mainly due to the shortening of the cardiac cycle, not due to the increase of the stoke volume. The cardiac work over one cardiac cycle increases little as the stroke volume and the operating pressure range of the left ventricle does not increase much. However, the cardiac work over a fixed duration of time is greater for the light exercise condition resulting from the shortened cardiac cycle.

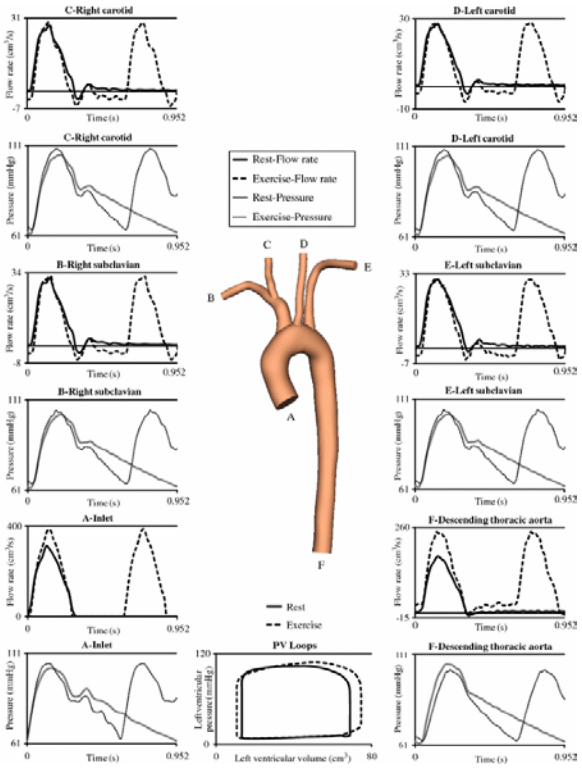

Figure 4 Computed pressure and flow waveforms at the inlet and the outlet boundaries at rest and during exercise. Also shown are the corresponding pressure–volume loops of the left ventricle

Figure 4 shows that the upper branch vessels experience retrograde flow in diastole. Retrograde flow to the upper branch vessels becomes severe in the light exercise condition even though the same boundary conditions were assigned to the upper branch vessels likely due to the increased flow demand to the descending thoracic aorta. The descending thoracic aorta has positive flow in diastole. Figure 4 also shows the pressure waveforms of the upper branch vessels and the descending thoracic aorta. The pressure waveform of the descending thoracic aorta decays faster during exercise compared to the resting condition.

In Fig. 5, volume rendered velocity magnitudes are shown for peak systole, late systole, and mid-diastole in order to illustrate complex flow features in the thoracic aorta resulting from the high inertia of blood traveling through the arch and the presence of the great vessels. Note the different scales for mid-diastole. These complex flow features are more pronounced in late systole when the aortic flow is decelerating. For the light exercise condition, positive flow to the descending thoracic aorta in diastole resulted in persistent flow complexity compared to the resting condition (Fig. 5C and c).

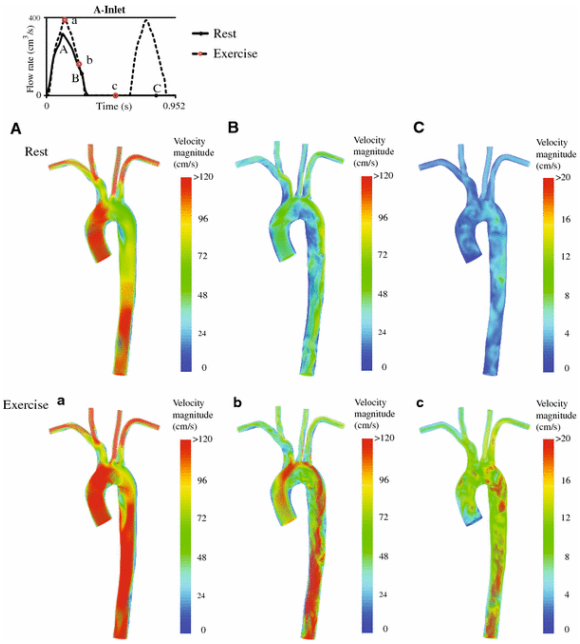

Figure 5 Volume rendered velocity magnitude in a normal thoracic aorta at three different time points at rest and during exercise. Note the different scales for mid-diastole

Mean wall shear stress and oscillatory shear index for the resting condition and the light exercise condition are also plotted in Fig. 6. For the light exercise condition, mean wall shear stress increased as a higher flow was ejected from the left ventricle. Few zones with shear stress less than 10 dynes/cm^2 remain with exercise. The oscillatory shear index for the light exercise condition was decreased in the descending thoracic aorta as the descending thoracic aorta had higher flow but increased in the upper branch vessels as these vessels experienced higher retrograde flow in diastole.

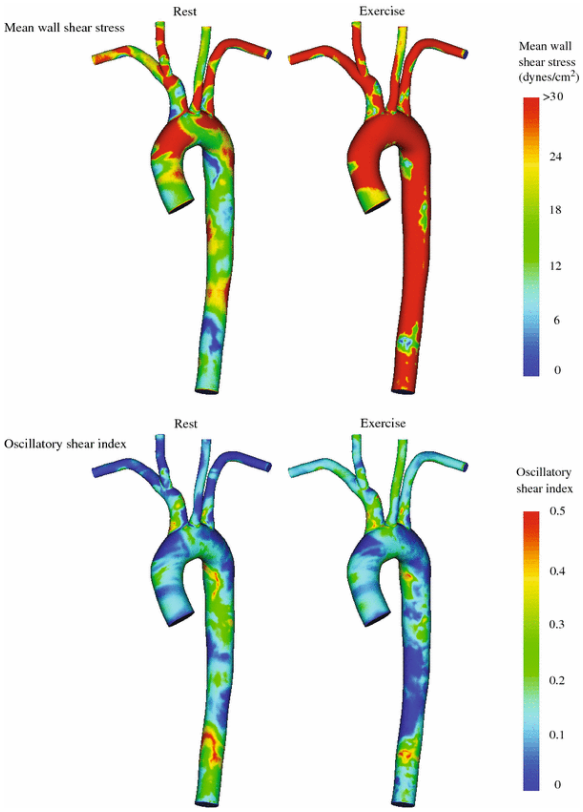

Figure 6 Mean wall shear stress and oscillatory shear index of a normal thoracic aorta at rest and during exercise

A Thoracic Aorta Model with an Aortic Coarctation at Pre-Intervention and Post-Intervention

In these simulations, we studied how the afterload changes as a coarctation in the descending thoracic aorta is removed. We constructed a subject-specific thoracic aorta model of a ten-year-old female subject with an aortic coarctation (Fig. 7). For the pre-intervention case, when the aortic coarctation is still present, the solutions were obtained using a 2,647,619 element and 475,866 node mesh with a time step size of 0.025 ms. Note that a small time step size was chosen to adequately resolve the complex flow features distal to the aortic coarctation. The shape of the velocity profiles at the inlet and all the outlets was constrained to an axisymmetric shape with a profile order of six. The parameter values of the Windkessel models are shown in Fig. 7 along with the time-varying elastance function and the parameter values of the lumped parameter heart model. A constant Young's modulus for the vessel wall was chosen to be 8.78×10^6 dynes/cm^2 so that a maximum deformation of 10% was obtained. This matched the wall deformation at the level of the ascending and the descending thoracic aorta based on cine PC-MRI data.

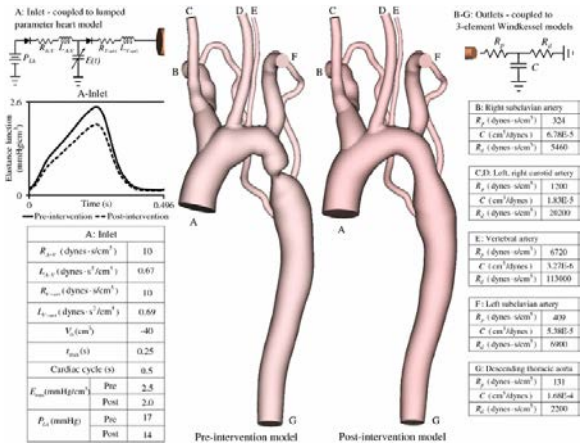

Figure 7 Problem specification for simulations of blood flow in a subject-specific thoracic aorta model with an aortic coarctation under pre-intervention and simulated post-intervention conditions. To highlight the effect of treatment of the coarctation, outlet boundary conditions are unchanged from the pre-intervention to post-intervention state

To simulate a post-intervention case, a “virtual surgery” was performed computationally by translating and joining the aorta proximal and distal to the coarctation using surgical guidelines.13 The solutions of the post-intervention case were obtained using a 2,501,074 element and 449,968 node mesh with a time step size of 0.13 ms. We ran two separate simulations for the post-intervention case. First, we maintained the same contractility of the left ventricle to simulate blood flow and pressure right after removing the coarctation in the descending thoracic aorta. Second, we decreased the maximum elastance value, representing the contractility of the left ventricle, until the computed cardiac output matched the cardiac output measured for the pre-intervention case to approximate the autoregulatory mechanisms of the cardiovascular system. To highlight the effect of treatment of the coarctation, the outlet boundary conditions were unchanged from the pre-intervention case to the post-intervention case. The same value of Young’s modulus was used for the post-intervention simulation. For the pre-intervention and post-intervention cases, simulations were run for up to six cardiac cycles, until the flow rate and pressure fields yielded periodic solutions.

In Fig. 8, computed flow and pressure waveforms of the inlet and outlets and pressure–volume loops of the left ventricle are shown for the pre-intervention case and two post-intervention cases. The measured cardiac output of the subject was 6.5 L/min for the pre-intervention case. The computed cardiac output of the subject was 6.7 L/min for the pre-intervention case, 8.1 L/min for the post-intervention case with the same contractility of the left ventricle, and 6.5 L/min for the post-intervention case with the decreased contractility of the left ventricle. These values for the resting condition are within the normal cardiac output range for children with an aortic coarctation when scaled to body surface area. The body surface area for this patient was 0.93 m^2 with the preoperative cardiac index of 7.18 L/min/m^2 and the postoperative cardiac index of 6.98 L/min/m^2.22 The cardiac output computed from these cardiac indices was 6.7 L/min for the pre-intervention case and 6.5 L/min for the post-intervention case. The measured brachial pulse pressure of the ten-year-old subject before the intervention ranged from 68 to 142 mmHg. The computed left subclavian pulse pressure of the subject ranged from 65 to 144 mmHg for the pre-intervention case, from 101 to 137 mmHg for the post-intervention case with the same contractility, and from 86 to 127 mmHg for the post-intervention case with the reduced contractility. The computed descending thoracic aortic pulse pressure of the subject ranged from 63 to 90 mmHg for the pre-intervention case, from 100 to 130 mmHg for the post-intervention case with the same contractility, and from 85 to 110 mmHg for the post-intervention case with the reduced contractility. The computed pulse of the left subclavian artery changed from 79 mmHg to 36 and 41 mmHg, respectively, as the resistance at the aortic coarctation was relieved. The maximum inflow rate increased as observed in Fig. 8. Also, the flow waveforms at

the descending thoracic aorta demonstrate increased pulsatility as the coarctation is removed. Cardiac work was computed using a trapezoidal integration scheme. For the pre-intervention case, the computed cardiac work was 6900 mmHg cm^3. However, after finding a new homeostatic state after the surgery, the computed cardiac work was 5900 mmHg cm^3. The cardiac work of the left ventricle was therefore acutely reduced by 14% relative to the pre-intervention level.

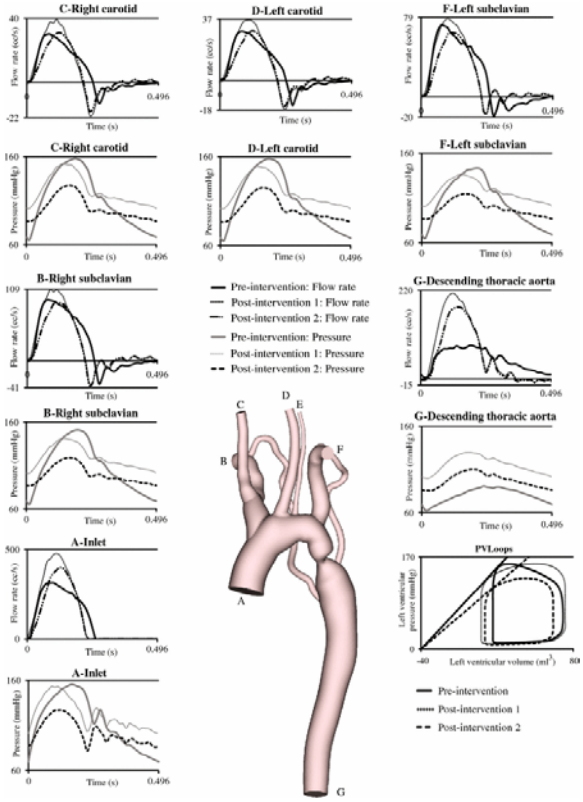

Figure 8 Computed pressure and flow waveforms at the inlet and selected outlet boundaries of an aortic coarctation model for pre-intervention and post-intervention conditions. Post-intervention case 1 represents the changes that would occur with relief of the aortic coarctation, but no change in contractility whereas post-intervention case 2 models a decrease in contractility until the cardiac output matches that of the pre-intervention case. Also shown are the corresponding pressure–volume loops of the left ventricle. Note the change in the slope shown on the pressure–volume diagram. This slope is related to the end systolic pressure–volume relationship (ESPVR) and therefore represents the reduction in contractility achieved by relieving the aortic coarctation

In Fig. 9, volume rendered velocity magnitudes are shown for peak systole, late systole, and mid-diastole for pre-intervention case and the post-intervention case after reaching a new homeostatic state. Note the different scales for mid-diastole. High velocity is observed at the coarctation for the pre-intervention case. Flow below the aortic coarctation becomes chaotic, especially in the deceleration phase and this complex flow feature disappears slowly in diastole.

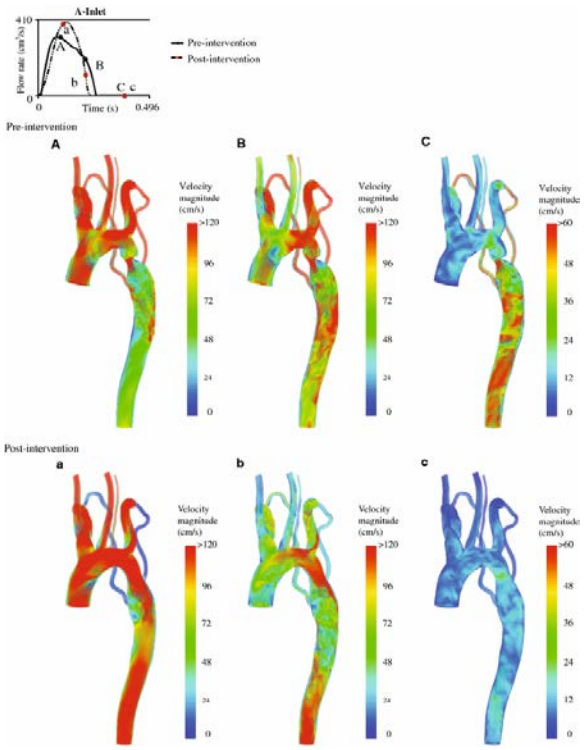

Figure 9 Volume rendered velocity magnitude in a thoracic aorta with an aortic coarctation at three different time points for pre-intervention condition and post-intervention condition representing the new homeostatic state. Note the different scales for mid-diastole

Figure 10 shows pressure contours for peak systole, late systole, and mid-diastole for pre-intervention case and the post-intervention case after reaching a new homeostatic state. Note the fact that pressure proximal to the coarctation is higher during the deceleration phase of systole than at peak systole. We can observe a large pressure loss in the pre-intervention case due to the coarctation of the aorta. The large pressure loss disappears for the two post-intervention cases. The operating pressure range is also higher for the pre-intervention case compared to the post-intervention case after reaching a new homeostatic state.

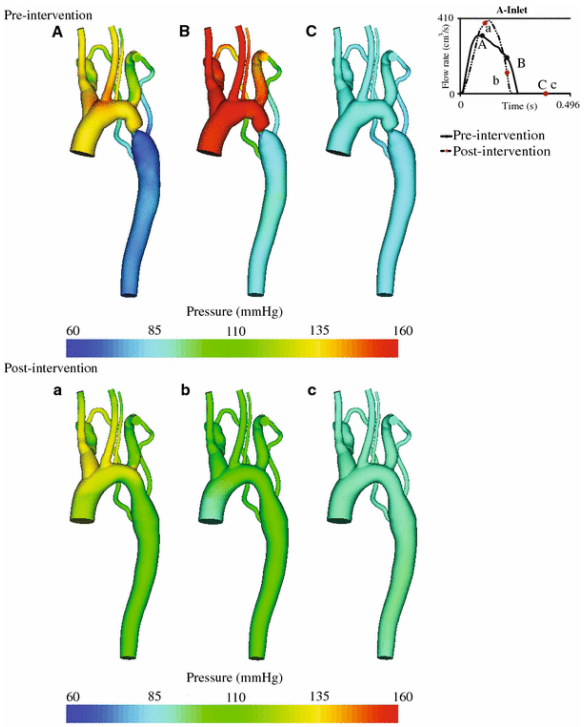

Figure 10 Pressure contours in a thoracic aorta with an aortic coarctation at three different time points for pre-intervention condition and post-intervention condition representing the new homeostatic state. Note the fact that pressure proximal to the coarctation is higher during the deceleration phase of systole than at peak systole

Discussion

We have successfully developed and implemented an inflow boundary condition that couples a lumped parameter heart model to the inlet of a three-dimensional finite element model of the aorta. We also used deformable wall properties developed in prior work to better represent flow and pressure waveforms. Because we considered deformable wall properties, when the aortic valve was open, the only Dirichlet boundary conditions were the inlet and outlet rings for each computational domain. While previous work found that flow simulations with few Dirichlet boundary conditions are unstable,8 our method is robust and stable due to the constraints on the shape of the velocity profiles at the inlet and the outlets of the computational domain.

Using the lumped parameter heart model as an inflow boundary condition, we studied how changes in cardiac properties affect the arterial system and vice versa. We simulated two different physiologic conditions, first with a normal thoracic aorta model, and then with a thoracic aorta model with an aortic coarctation.

For the normal thoracic aorta model, we simulated rest and light exercise conditions. To simulate a light exercise condition, we only shortened the cardiac cycle until we recovered the same systolic pressure after decreasing the resistance of the lower extremities. In reality, systolic pressure should be higher depending on the degree of exercise but in this simulated light exercise case, we did not consider the increase in the systolic pressure. From the simulation results, we observed that shortening the cardiac cycle can increase cardiac output significantly without changing the contractility of the heart, and still maintain physiologic pressures despite reductions in vascular resistance. We also observed that, during exercise, a faster pressure decay due to the lower resistance to flow in the lower extremities augments ejection of blood from the heart during late systole. Flow in the lower extremities increased significantly, causing higher retrograde flow in the upper branch vessels. For the aortic coarctation model, we computed afterload for the pre-intervention and post-intervention cases. As the coarctation was removed for the post-intervention case, the total resistance of the arterial system was reduced,

relieving the afterload of the left ventricle and the contractility of the left ventricle was reduced accordingly. In the pre-intervention case, although the measurement was made in a resting state, the left ventricle had a short cardiac cycle with high cardiac output, emulating an exercise condition of a normal subject, a commonly reported finding for patients with a native (i.e., uncorrected) aortic coarctation.34 To simulate the post-intervention case, we decreased the maximum elastance value until we obtained the same cardiac output, approximating the autoregulatory mechanisms in the cardiovascular system. Patients with an aortic coarctation generally experience a decrease in the cardiac output in addition to a decrease in the maximum elastance value after removing the coarctation.34 Yet, in this study, we only changed the maximum elastance value assuming that the patient maintains the same cardiac output. From the simulation results, we observed that the operating pressure range for the post-intervention case was lower compared to the pre-intervention case, signifying a reduction in the afterload of the left ventricle.

We have shown that this method can be used to study the interactions between the heart and the arterial system. However, this study has three primary limitations. First, feedback control loops were not present in the computational domain. Different physiologic conditions simulated in this paper were all modeled by manually changing the parameter values of the lumped parameter heart model based on literature data. To replicate physiologic changes due to changes in the heart function or arterial impedance, the development of feedback control loops and models of the autoregulatory mechanisms of the cardiovascular system are needed.

Second, the tuning of the parameter values of the lumped parameter heart model was complex and time consuming. When the lumped parameter heart model was implemented as an inflow boundary condition of a three-dimensional finite element model of the aorta, several parameter values were introduced and adjusted to match subject-specific pulse pressure and cardiac output through an iterative approach. To expedite the study of the interactions between the heart and the arterial circulation, automatic optimization of these parameter values is necessary.

Third, uniform deformable wall properties were assigned to each computer model despite the fact that the vessel wall properties vary spatially. To compute flow and pressure waveforms considering non-uniform vessel wall properties, noninvasive methods to estimate wall thickness and elastic (viscoelastic) wall properties are needed. Additionally, the current deformable wall model does not consider bending stiffness. The absence of bending stiffness in the deformable wall model resulted in oscillations of the flow and pressure waveforms due to the high inertia of blood flow traveling through the arch of the aorta. More realistic deformable wall models with consideration of bending stiffness may reduce the amplitude of these oscillations.

Conclusions

We have successfully implemented an inflow boundary condition coupling a lumped parameter heart model to the inlet of a three-dimensional finite element model of the aorta. Although we only modeled the left side of the heart and the systemic circulation, the same approach can be applied to the right side of the heart and the pulmonary circulation. We have shown that interactions between the heart and the systemic circulation can be studied using this method. This approach can be applied to better understand human physiology including how changes in the arterial system affect cardiac properties or vice versa. It can also be utilized to predict outcomes of cardiovascular interventions as demonstrated with the patient-specific thoracic aorta model with an aortic coarctation.

References

1. Asanoi, H., T. Kameyama, S. Ishizaka, T. Nozawa, and H. Inoue. Energetically optimal left ventricular pressure for the failing human heart. *Circulation* 93(1):67–63, 1996.

2. Brooks, A. N., and T. J. R. Hughes. Streamline upwind/Petrov-Galerkin formulations for convection dominated flows with particular emphasis on the incompressible Navier-Stokes equations. *Comput. Methods Appl. Mech. Eng*. 32:199–259, 1982.
3. Cebral, J. R., M. A. Castro, J. E. Burgess, R. S. Pergolizzi, M. J. Sheridan, and C. M. Putman. Characterization of cerebral aneurysms for assessing risk of rupture by using patient-specific computational hemodynamics models. *AJNR Am. J. Neuroradiol*. 26(10):2550–2559, 2005.
4. Figueroa, C. A., I. E. Vignon-Clementel, K. E. Jansen, T. J. R. Hughes, and C. A. Taylor. A coupled momentum method for modeling blood flow in three-dimensional deformable arteries. *Comput. Methods Appl. Mech. Eng*. 195(41–43):5685–5706, 2006.
5. Formaggia, L., J. F. Gerbeau, F. Nobile, and A. Quarteroni. On the coupling of 3D and 1D Navier-Stokes equations for flow problems in compliant vessels. *Comput. Methods Appl. Mech. Eng*. 191(6–7):561–582, 2001.
6. Formaggia, L., D. Lamponi, M. Tuveri, and A. Veneziani. Numerical modeling of 1D arterial networks coupled with a lumped parameters description of the heart. *Comput. Meth. Biomech. Biomed. Eng*. 9(5):273–288, 2006.
7. Franca, L. P., and S. L. Frey. Stabilized finite element methods: II. The incompressible Navier-Stokes equations. *Comput. Methods Appl. Mech. Eng*. 99(2–3):209–233, 1992.
8. Heywood, J., R. Rannacher, and S. Turek. Artificial boundaries and flux and pressure conditions for the incompressible Navier-Stokes equations. *Int. J. Numer. Methods Fluids* 22(5):325–352, 1996.
9. Hope, S. A., D. B. Tay, I. T. Meredith, and J. D. Cameron. Waveform dispersion, not reflection, may be the major determinant of aortic pressure wave morphology. *Am. J. Physiol. Heart Circ. Physiol*. 289(6):H2497–H2502, 2005.
10. Hunter, P. J., A. J. Pullan, and B. H. Smaill. Modeling total heart function. *Annu. Rev. Biomed. Eng*. 5(1):147–177, 2003.
11. Kerckhoffs, R. C. P., M. L. Neal, Q. Gu, J. B. Bassingthwaighte, J. H. Omens, and A. D. McCulloch. Coupling of a 3D finite element model of cardiac ventricular mechanics to lumped systems models of the systemic and pulmonic circulation. *Ann. Biomed. Eng*. 35(1):1–18, 2007.
12. Kim, H. J., C. A. Figueroa, T. J. R. Hughes, K. E. Jansen, and C. A. Taylor. Augmented lagrangian method for constraining the shape of velocity profiles at outlet boundaries for three-dimensional finite element simulations of blood flow. *Comput. Methods Appl. Mech. Eng*. (in press). doi:10.1016/j.cma.2009.02.012
13. Kirklin, J. W., and B. G. Barratt-Boyes. Cardiac Surgery: Morphology, Diagnostic Criteria, Natural History, Techniques, Results, and Indications, 2nd edition. New York: W.B. Saunders, 1993.
14. Laskey, W. K., H. G. Parker, V. A. Ferrari, W. G. Kussmaul, and A. Noordergraaf. Estimation of total systemic arterial compliance in humans. *J. Appl. Physiol*. 69(1):112–119, 1990.
15. Li, Z., and C. Kleinstreuer. Blood flow and structure interactions in a stented abdominal aortic aneurysm model. *Med. Eng. Phys*. 27(5):369–382, 2005.
16. Migliavacca, F., R. Balossino, G. Pennati, G. Dubini, T. H. Hsia, M. R. de Leval, and E. L. Bove. Multiscale modelling in biofluidynamics: application to reconstructive paediatric cardiac surgery. *J. Biomech*. 39(6):1010–1020, 2006.
17. Ottesen, J. T., M. S. Olufsen, and J. K. Larsen. Applied Mathematical Models in Human Physiology. SIAM Monographs on Mathematical Modeling and Computation. Philadelphia: SIAM, 2004.
18. Perktold, K., R. Peter, and M. Resch. Pulsatile non-Newtonian blood flow simulation through a bifurcation with an aneurysm. *Biorheology* 26(6):1011–1030, 1989.
19. Quarteroni, A., S. Ragni, and A. Veneziani. Coupling between lumped and distributed models for blood flow problems. *Comput. Vis. Sci*., 4(2):111–124, 2001.
20. Sahni, O., J. Muller, K. E. Jansen, M. S. Shephard, and C. A. Taylor. Efficient anisotropic adaptive discretization of the cardiovascular system. *Comput. Methods Appl. Mech. Eng*. 195(41–43):5634–5655, 2006.

21. Sainte-Marie, J., D. Chapelle, R. Cimrman, and M. Sorine. Modeling and estimation of the cardiac electromechanical activity. *Comput. Struct*. 84:1743–1759, 2006.
22. Seear, M., S. Webber, and J. Leblanc. Descending aortic blood flow velocity as a noninvasive measure of cardiac output in children. *Pediatr. Cardiol*. 15(4):178–183, 1994.
23. Segers, P., N. Stergiopulos, and N. Westerhof. Relation of effective arterial elastance to arterial system properties. *Am. J. Physiol. Heart Circ. Physiol*. 282(3):H1041–H1046, 2002.
24. Segers, P., N. Stergiopulos, N. Westerhof, P. Wouters, P. Kolh, and P. Verdonck. Systemic and pulmonary hemodynamics assessed with a lumped-parameter heart-arterial interaction model. *J. Eng. Math*. 47(3):185–199, 2003.
25. Senzaki, H., C. H. Chen, and D. A. Kass. Single-beat estimation of end-systolic pressure-volume relation in humans: a new method with the potential for noninvasive application. *Circulation* 94(10):2497–2506, 1996.
26. Soerensen, D. D., K. Pekkan, D. de Zelicourt, S. Sharma, K. Kanter, M. Fogel, and A. P. Yoganathan. Introduction of a new optimized total cavopulmonary connection. *Ann. Thorac. Surg*. 83(6):2182–2190, 2007.
27. Stergiopulos, N., P. Segers, and N. Westerhof. Use of pulse pressure method for estimating total arterial compliance in vivo. *Am. J. Physiol. Heart Circ. Physiol*. 276(2):H424–H428, 1999.
28. Stuhne, G. R., and D. A. Steinman. Finite-element modeling of the hemodynamics of stented aneurysms. *J. Biomech. Eng*. 126(3):382–387, 2004.
29. Suga, H., and K. Sagawa. Instantaneous pressure-volume relationships and their ratio in the excised, supported canine left ventricle. *Circ. Res*. 35(1):117–126, 1974.
30. Tang, B. T., C. P. Cheng, M. T. Draney, N. M. Wilson, P. S. Tsao, R. J. Herfkens, and C. A. Taylor. Abdominal aortic hemodynamics in young healthy adults at rest and during lower limb exercise: quantification using image-based computer modeling. *Am. J. Physiol. Heart Circ. Physiol*. 291(2):H668–H676, 2006.
31. Taylor, C. A., and M. T. Draney. Experimental and computational methods in cardiovascular fluid mechanics. *Annu. Rev. Fluid Mech*. 36(1):197–231, 2004.
32. Taylor, C. A., M. T. Draney, J. P. Ku, D. Parker, B. N. Steele, K. Wang, and C. K. Zarins. Predictive medicine: computational techniques in therapeutic decision-making. *Comput. Aid. Surg*. 4(5):231–247, 1999.
33. Taylor, C. A., T. J. R. Hughes, and C. K. Zarins. Finite element modeling of blood flow in arteries. *Comput. Methods Appl. Mech. Eng*. 158(1–2):155–196, 1998.
34. Taylor, S. H., and K. W. Donald. Circulatory studies at rest and during exercise in coarctation of the aorta before and after operation. *Br. Heart J*. 22:117–139, 1960.
35. Vignon-Clementel, I. E., C. A. Figueroa, K. E. Jansen, and C. A. Taylor. Outflow boundary conditions for three-dimensional finite element modeling of blood flow and pressure in arteries. *Comput. Methods Appl. Mech. Eng*. 195(29–32):3776–3796, 2006.
36. Whiting, C. H., and K. E. Jansen. A stabilized finite element method for the incompressible Navier-Stokes equations using a hierarchical basis. *Int. J. Numer. Methods Fluids* 35(1):93–116, 2001.
37. Zamir, M., P. Sinclair, and T. H. Wonnacott. Relation between diameter and flow in major branches of the arch of the aorta. *J. Biomech*. 25(11):1303–1310, 1992.

Acknowledgments

Hyun Jin Kim was supported by a Stanford Graduate Fellowship. This material is based upon work supported by the National Science Foundation under Grant No. 0205741. The authors gratefully acknowledge Dr. Nathan M. Wilson for assistance with software development. The authors gratefully acknowledge Dr. Farzin Shakib for the

use of his linear algebra package AcuSolve™ (http://www.acusim.com) and the support of Simmetrix, Inc for the use of the MeshSim™ (http://www.simmetrix.com) mesh generator.